Long-Term Field Screening by Mobile Ions in Thick Metal Halide Perovskites: Understanding Saturation Currents

Osbel Almora,* Daniel Miravet, Ilario Gelmetti, and Germà Garcia-Belmonte*

Metal halide perovskite-based semiconductor devices with micrometer-to-millimeter-thick perovskite layers show a current response upon polarization which evolves up to several hours, transiting several regimes. This is the case of X-ray detectors where the use of absorber perovskites produces instabilities in the dark reverse saturation current hindering the signal processing. Even though these phenomena are often attributed to the electronic–ionic conductivity and the interface phenomena in these perovskites, a proper theoretical description is missing. Herein, the numerical simulation study reproduces the main experimental trends and explains the origin of some of the apparently-always-increasing current transients in thick perovskite samples. The mobile ion concentration and mobility are correlated with three main transport regimes and interpretation and parameterization are provided to the current saturation time in terms of the ionic screening of the electric field toward the interfaces. The final steady-state under reverse polarization is found as diffusion-limited electronic current, which results from abrupt mobile ion depletion proportional to the Debye length in the vicinity of a contact. The conclusions suggest the material optimization of the contact interfaces as a pathway to reduce the long current saturation times in these devices.

1. Introduction

The material family of the lead halide perovskites has gained significant attention for application as potential absorbers for X-ray detection.[1,2] The favorable optoelectronic properties and the relatively easy and low-cost fabrication methods for these materials have already proven unprecedented progress among photovoltaic devices in terms of power conversion efficiency.[3] However, the dual ionic–electronic conductivity of the halide perovskites persists as a challenge for the understanding and progress of these devices.[4,5] The mobile ions not only relate to the anomalous hysteresis of the current density–voltage (J–V) curve,[6–8] but also affect the current long-term stability.[9–11] The long-term steadiness of current is of particular importance for perovskite-based X-ray detectors (PXDs) where the typical operational mode implies monitoring the photocurrent at a given reverse bias voltage with respect to the reference dark current.

For lead halide perovskite-based ionizing energy detectors, where the absorber thickness L ranges up to millimeters thick, the dark currents have been reported to have a time (t) evolution toward saturation during hours.[9–11] Interestingly, such a behavior includes several regimes. **Figure 1**a shows a representative experimental chronoamperometry from our previous work[12] and Figure 1b schemes the corresponding three main current domains. First, upon application of bias voltage there is i) the electronic charge carrier response in a time scale up to the order of microseconds. This may be either the typical ohmic response or a slower trap-mediated process during a time window where no significant change is made to the ionic charge density profile. Note that this regime (i) is not shown in Figure 1a for practical experimental reasons and it will similarly be neglected along the below simulations due to numerical simplification. Subsequently, ii) the activation of ionic–electronic current occurs when the ionic migration current competes with

O. Almora, G. Garcia-Belmonte
Institute of Advanced Materials (INAM)
Universitat Jaume I
12006 Castelló, Spain
E-mail: oalmora@upo.es; garciag@uji.es

O. Almora
Erlangen Graduate School in Advanced Optical Technologies (SAOT)
Friedrich-Alexander Universität Erlangen-Nürnberg
Erlangen 91052, Germany

O. Almora
Universidad Pablo de Olavide
41013 Seville, Spain

D. Miravet
Advanced Research Complex ARC
Department of Physics
University of Ottawa
Ottawa, ON K1N 6N5, Canada

I. Gelmetti
Institute of Chemical Research of Catalonia (ICIQ)
The Barcelona Institute of Science and Technology (BIST)
Tarragona 43007, Spain

ADVANCED
SCIENCE NEWS

www.advancedsciencenews.com
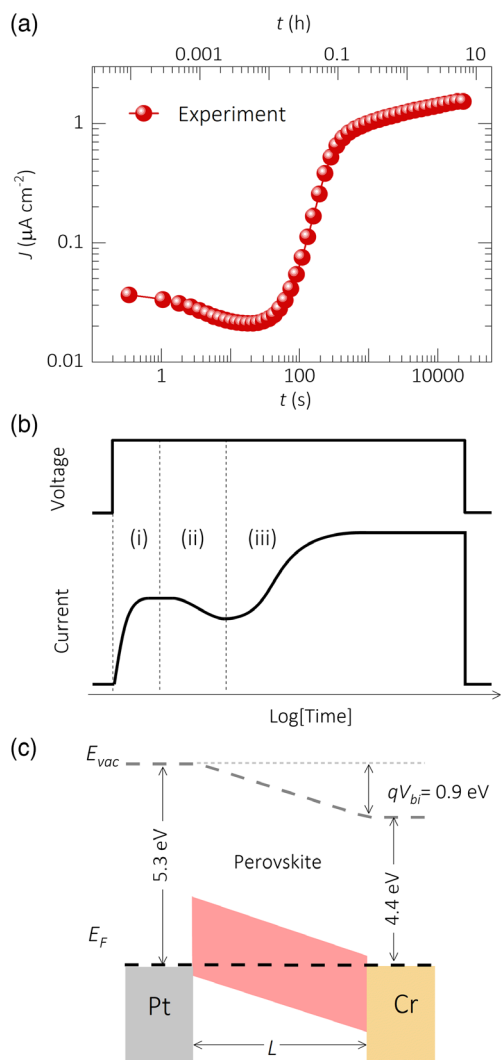
pss
physica
status
solidi
rrl

www.pss-rapid.com

Figure 1. a) Experimental time evolution of the absolute current density for a 831 µm-thick MAPbI$_3$-based X-ray detector at −5 V, in dark and with N$_2$ atmosphere. Adapted with permission.[12] Copyright 2022, Wiley-VCH. b) Schemed regimes of long-term dark reverse bias current response to polarization: i) fast electronic response, ii) ionic–electronic current activation, and iii) saturation toward steady-state electronic current. c) Energy diagram for the simulation of the perovskite-based X-ray detectors, where E_{vac} is the vacuum level, E_F is the Fermi level, and qV_{bi} is the built-in voltage energy.

parameterization and quantification of the phenomena is still missing. Furthermore, the shape of each regime has been found to depend on the voltage bias and nearly linear trends ($J \propto V^n$, $n \approx 1$) have been reported for the saturation current.[10–12,14]

The drift-diffusion numerical simulations are arguably the most exhaustive parameterization approach to understand the macroscopic electrical response of semiconductor devices. For decades, the numerical tools for the mostly stationary solutions of the transport equations have been well developed for devices composed by classic inorganic semiconductors[15–18] and organic materials.[19,20] However, the emergence of metal halide perovskites required the inclusion of the time dependency and the dual electronic–ionic conductivity with a primary focus on the hysteresis phenomena of the J–V curve of perovskite solar cells.[13,21–27] Further development has also been reported for the simulation of voltage[28] and current[29–31] transients, and impedance spectroscopy[13,31,32] measurements similarly influenced by slower mobile ion-related processes. Yet, these studies tackle photovoltaic devices where typical perovskite thicknesses are in the order of 500 nm and the time scale of the electrical response is up to minutes.

In this work, a numerical simulation study of the up-to-tens-of-hours reverse bias current response of PXDs is presented. The studied devices follow the simple Schottky-diode-like configuration from previous works[10,33] where up-to-millimeter-thick perovskite pellets are sandwiched between metals of different work function (WF), as schemed in Figure 1c. For the numerical simulations, the open source MATLAB code Driftfusion[34] was employed. Our results indicate the importance of interface phenomena and field screening behind the slow kinetics of thick PXDs.

2. Theoretical Assumptions for Initial and Boundary Conditions

For a start, the simulations were made within the framework of Driftfusion,[34] including both radiative and nonradiative recombination, and taking four main assumptions. First, the bulk of the perovskite is initially taken as intrinsic. This means that the total equilibrium concentrations of fixed and mobile ions should be balanced, i.e., same total number of cations and anions (our simulation case), or effectively in the order of the intrinsic concentration (possible experimental situation). Second, the interface regions between the perovskite and the contacts are unintendedly doped, forming depletion layers with thicknesses in the order of tens of nanometers. This is presented in the illustrative initial charge density profile of Figure S1, Supporting Information, where nanometer-thin layers are set toward the interfaces with more than 20 orders of magnitude difference between concentrations of majority and minority charge carriers. Third, only one type of mobile ions is considered to effectively contribute to the current and the reordering of the charge density profile. Finally, the built-in field forming the Schottky-diode-like detector is only defined by the difference in WF between the two metals. The following simulations consider chromium and platinum electrodes (see Figure 1c), as used in our previous experimental works,[10,33] whose WF mismatch (see Table S1, Supporting Information) can be assumed to result in a

the continuous electronic current and/or when the ionic reordering of the charge density profile makes changes in the electrostatic potential (φ) larger than the thermal fluctuation ($k_B T/q$) which modify the flux of electronic charge carriers. Finally, and closely linked to the previous regime, a iii) saturation to the steady-state electronic current arises when the ionic migration currents are no longer significant, and the ionic charge density profile reaches steady state. Note that the ionic migration current has also been referred to as ionic displacement current[13] because they are proportional to the time variation of the electric field. However, despite a phenomenological description of the current time evolution has been proposed, a proper

built-in potential of $V_{bi} = 0.9$ V. An illustrative set of simulation parameters is presented in Table S2, Supporting Information, and a comprehensive explanation of the use and setting up the Driftfusion code can be found in the original publication.[34] A representative initial equilibrium charge density profile is presented in Figure S1, Supporting Information, which corresponds to the concentration values for each stand-alone layer before the device equilibrium profile when the interfaces are contacted.

Notably, the solution of the time-dependent set of continuity and Poisson equations for electronic and mobile ions is particularly challenging due to the contrasting time and space scales related to these two types of charge carriers. While the electrons and holes respond in the order from nano- to microseconds, it takes up to hours for the mobile ions to effectively contribute to the current response. In addition, the thicker the perovskite layer, the higher is the contrast between the bulky and interface phenomena. These issues constitute significant complications for the convergence of the numerical solutions, which limit some parameter to be tested in wider ranges.

3. Results and Discussion

3.1. Effects of Field, Ion Concentration, and Ion Mobility

The simplest experiment to test the long-term current response of PXDs is the measurement of chronoamperometries at different polarizations, i.e., repeating the protocol schemed in Figure 1b for different long-term voltage pulses, as in our previous works.[10–12,14] The corresponding simulations can be found in **Figure 2**a and S2a, Supporting Information, for different ranges of mobile ion concentration (N_{ion}) and mobility (μ_{ion}). Similarly, the effect of changing N_{ion} and μ_{ion} is presented in Figure 2b,c, respectively. All the simulations show nearly constant currents within the ranges from milliseconds to seconds and after the saturation, hours later. A comparison between these two characteristic current levels, corresponding to the ion activation (ii) and saturation (iii) regimes, is presented in Figure 2d–f. Moreover, Figure 2d–f also indicates the corresponding ohmic ionic current $J = q \cdot N_{ion} \cdot \mu_{ion} \cdot V/L$, where q is the elementary
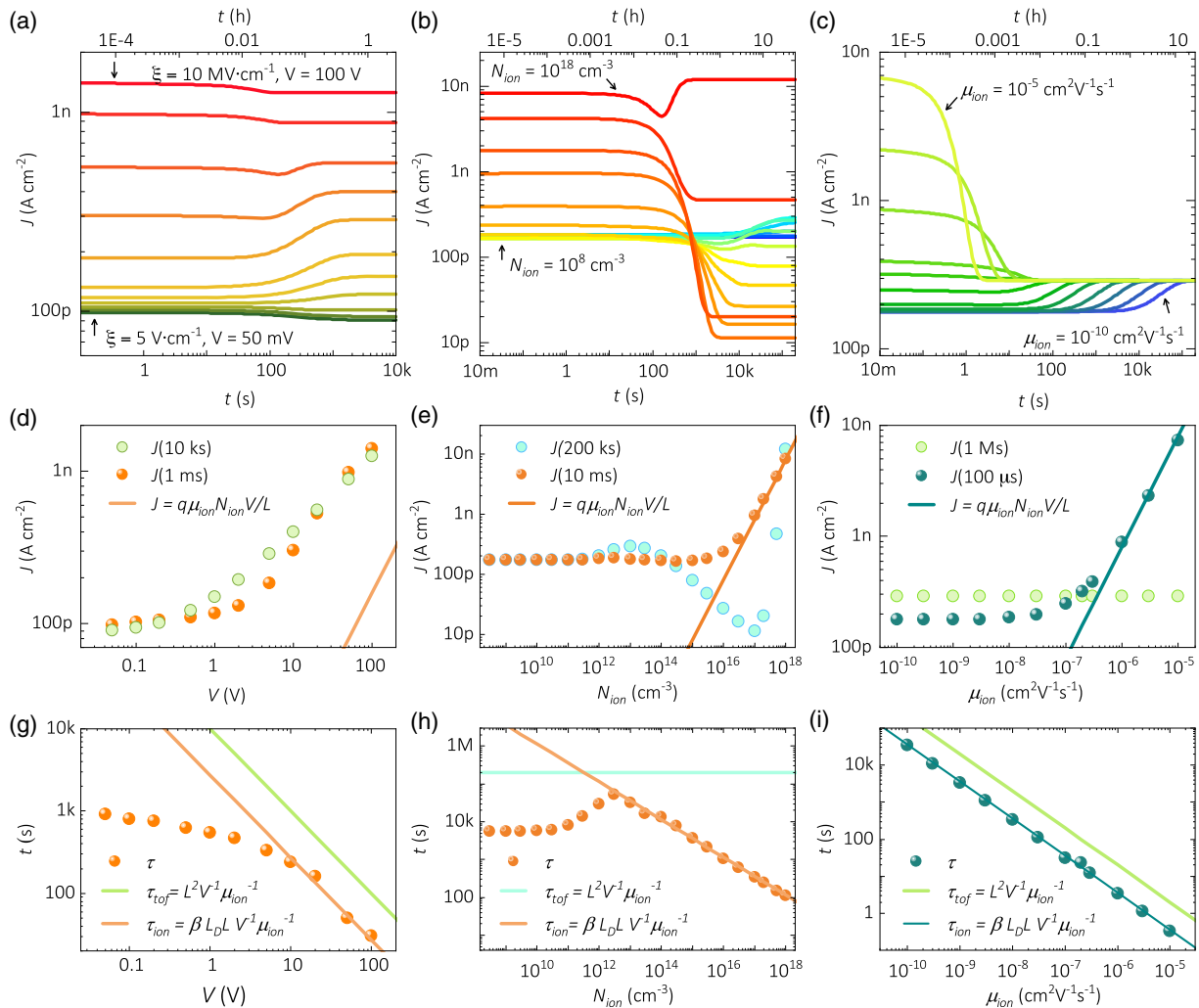

Figure 2. Simulated time evolution of absolute reverse current as a function of a) field, b) ion concentration, c) ion mobility, and corresponding behaviors for characteristic d–f) currents and g–i) times. Here, $L = 100\,\mu m$, $V = -5$ V in (b,c,e,f,h,i), $\beta = 15$ in (g), $\beta = 10$ in (h,i), $\mu_{ion} = 10^{-8}\,cm^2\,V^{-1}\,s^{-1}$ in (a,d,g), $\mu_{ion} = 10^{-10}\,cm^2\,V^{-1}\,s^{-1}$ in (b,e,h), and $N_{ion} = 10^{13}\,cm^{-3}$ in (a,c,d,f,g,i).

charge. Subsequently, the slowest characteristic time τ, corresponding to the saturation (iii) regime, was parameterized in each case with a single exponential decay function $J \propto \exp[-t/\tau]$ and the resulting values are in Figure 2g–i. Also in these figures, the τ values are put into perspective with respect to the mobile ion time of flight (τ_{tof}) for the ohmic and screened distributions of electric field (ξ). Provided the definition

$$\tau_{tof} = \frac{L}{\mu\xi} \cong \frac{Lw}{\mu V} \qquad (1)$$

For the ohmic situation, $w = L$ because the absolute field can be approximated as $\xi = \partial\varphi/\partial x \approx V/L$. However, in the presence of space charges the potential gradient is no longer distributed linearly in between the metal contacts but within smaller regions toward the electrodes. Then, a more suitable approximation would be $w = \beta \cdot L_D$ where β is a parameterization factor and the Debye length is defined as

$$L_D = \sqrt{\frac{\varepsilon_0 \varepsilon_r k_B T}{q^2 N_{ion}}} \qquad (2)$$

where ε_0 is the vacuum permittivity; ε_r is the dielectric constant; k_B is the Boltzmann constant, and T is the absolute temperature.

The field dependency in Figure 2a and S2a, Supporting Information, not only results in current trends such as the scheme of Figure 1b, but also indicates ranges where the ion activation (ii) regime shows a higher current than the final saturation (iii) regime. This is better illustrated in Figure 2d and S2b, Supporting Information, for low and high N_{ion} values, respectively. Notably, the saturation current (after hours) exhibits what seems to be the effect of transition between transport regimes as the voltage is varied in Figure 2d because no simple analytical function easily fits the voltage dependency. On the other hand, the ion-activation current (up to seconds) seems to transit from ionic–electronic at low N_{ion} to purely ionic for higher N_{ion} values, as shown in Figure S2b, Supporting Information. In terms of current saturation time, Figure 2g and S2s, Supporting Information, suggest that $w = \beta \cdot L_D \ll L$, meaning that the actual region where the effective field is distributed should be at least a vicinity of an electrode. Furthermore, we also simulated the current transients as a function of the perovskite thickness (see Figure S3, Supporting Information) to show the linear behavior of the saturation time and the distance between electrodes, in agreement with Equation (1).

The higher the mobile ion concentration, the higher is their effect on the long-term current–time evolution under polarization, as presented in Figure 2b,e,h. Similar to the voltage dependency, several ranges of N_{ion} can be found where the ion-activation current (ii) is below or above the saturation current (iii). Importantly, above a certain N_{ion} the ion-activation current is totally ionic, meaning that the electronic current in that time period is limited by the charge density profile at the moment. Furthermore, not only the saturation time is clearly found to depend on the mobile ion concentration, but also a trend $\tau \propto N_{ion}^{-1/2}$ is confirmed above a threshold concentration in Figure 2h. This dependency is also in agreement with the assumption of field screening and potential redistribution toward the electrodes within a region of thickness $w = \beta \cdot L_D$.

The ion mobility is shown to be a determining factor for the saturation time, but completely irrelevant for the saturation current in the simulations of Figure 2c,f,i. The saturation current does not change at all when varying the ion mobility, meaning that it is practically only composed by electronic charge carriers after the final reordering of the charge density profile. Contrastingly, Figure S4, Supporting Information, illustrates the strong dependency of the saturation current on the electronic mobility (linear at high N_{ion} values). Moreover, in the order of microseconds, the ion-activation current is only fully ionic above a threshold mobility value. Nevertheless, regardless of the ionic mobility range, the saturation time behaves as $\tau \propto \mu_{ion}^{-1}$, also in agreement with the $w = \beta \cdot L_D$ approximation.

Two elements that may influence the above simulations could be the presence of multiple mobile ion species and the variation of the recombination coefficients, specifically the trap assisted recombination lifetime. Even though the analyses of these instances are beyond the scope of the present study, one could speculate on some intuitive outcomes. Regarding the multiple mobile ion species, which may not be the most common case among typical materials for PXDs,[12] a superposition-like mechanism could take place. This implies that ion species with similar mobilities would hardly be discerned from each other, whereas ion species with significant difference in mobility would result in extra current transition regimes. Concerning the final charge density profile, mobile ions with the same charge sign should end up with distributions like those described in the following section. In contrast, mobile ions with opposite charge sign and similar concentration could pile up toward the corresponding electrode in a more symmetrical configuration. About the charge carrier nonradiative recombination, note that PXDs operate at reverse bias, which is the regime with the lowest contribution from recombination current at all. Having said that, exploring the effects due to different recombination coefficients should be comparable to the presented changes in mobile ion concentrations which consequently modified the electronic charge carrier densities and thus the recombination rates. More interesting would be the case where the mobile ions act as nonradiative recombination centers. This would require the ionic species to be present as midgap deep trap states rather than most typical doping-like shallow defects,[35,36] which could result in dissimilar responses to analyze in future works.

3.2. The Potential, Field, and Charge Density Profiles

The space distribution of the electrostatic potential, the electric field, and the concentration of charge carriers results in a transition from an ohmic-like situation to an asymmetric reordering with severely depleted regions, as illustrated in **Figure 3**. In the time scale up to the order of milliseconds, the electrostatic potential is almost linearly distributed along the bulk of the absorber perovskite (see Figure 3a). This implies that an effective constant field value could be approximated, even though there are clear maximum peaks toward the electrodes (see Figure 3b). Regarding the charge carrier density, a nearly symmetric disposition is found during the early stages of the ion activation regime, as shown in Figure 3c. The concentrations of electrons (n) and holes (p) show gradients in the first
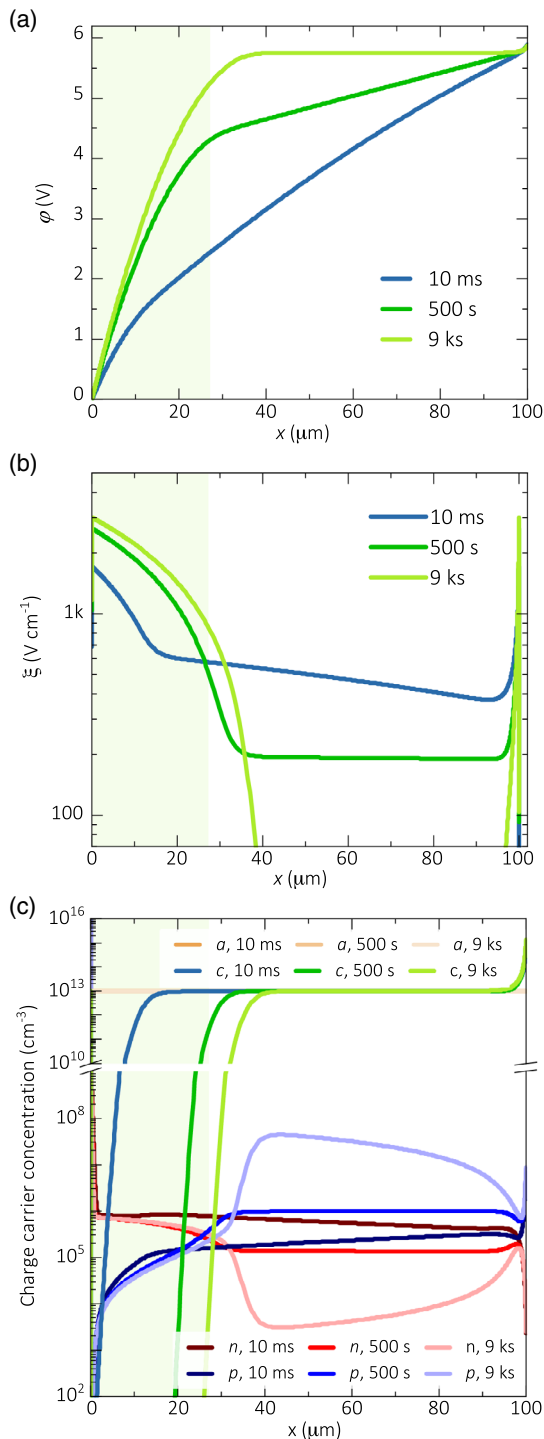
Figure 3. Simulated profiles for the internal a) electrostatic potential, b) the electric field, and c) the charge carrier densities as a function of time. Here, $L = 100\,\mu m$, $V = -5\,V$, $\mu_{ion} = 10^{-8}\,cm^2\,V^{-1}\,s^{-1}$, $N_{ion} = 10^{13}\,cm^{-3}$, and the highlighted area corresponds to the depletion region $w = \beta \cdot L_D$ with $\beta = 15$. In (c), a relates to anions, c to cations, n to electrons, and p to holes.

simulated sample time, whereas the mobile ions accumulate toward one electrode, depleting the opposite contact.

The longer the polarization time, the more the potential gradient locates in the proximity of one interface and the smaller the electric field in the bulk of the absorber perovskite. This leads to a depletion region of thickness $w = \beta \cdot L_D$ (green highlighted area in Figure 3) in the saturation time regime where a maximum field toward the contact triggers the electronic charge carrier density within the perovskite bulk. Markedly, this occurs while the mobile ion accumulation toward the opposite contact is not significantly changed because the equilibrium ion concentration already was around 100 times higher. As a result, the total current saturates toward a maximum (see Figure 2) because the depletion of mobile ions increases the bulk concentration of electronic charge carriers (holes in Figure 3). This bulk region with electronic concentration enhancement happens to also be nearly field-free, which suggests the electronic diffusion as a main transport mechanism for the saturation current.

Notably, it may result counterintuitive that the higher the reverse bias, the higher is the reverse current. However, there is no contradiction because the simulated concentration of mobile ions is taken in the order of, or higher than, the initial fixed self-doping concentration (see Figure S1, Supporting Information) and they accumulate (deplete) toward the interface with opposite (same) initial charge sign. In other words, reordered mobile ions invert the sign of the potential barriers in a way that the reverse biased device behaves similar to a forward bias regime. Therefore, provided the sufficient concentration of mobile ions, the effects of the initial potential barriers are negligible in comparison to the ionic reordering which define the saturation current and the final charge density profile. In addition, not only the initial field profile toward the interfaces is cancelled by the ion screening, but also the bulk electronic diffusion emerges as a main transport mechanism for the saturation current. For instance, Figure S5, Supporting Information, shows the experiments from our previous work,[10] where the current for reverse and forward biases converges toward a similar saturation value after 72 h of polarization, in spite of the initial different trends.

The extreme case where $w \ll L$ can be achieved either for sufficiently high perovskite thickness or mobile ion concentration. The latter is illustrated in the simulated profiles of Figure S6, Supporting Information, for $N_{ion} = 10^{18}\,cm^{-3}$, where the depletion region can only be observed with the logarithmic scale for the position axis. The electrostatic potential is practically linear within the bulk, meaning a corresponding constant electric field. The longer the polarization time, the smaller is the field within the perovskite bulk, but the higher toward the depleted contact. Moreover, an increase of electronic charge carrier density also occurs in the nearly field-free free region of the bulk due to the small depletion region for ionic (high depletion) and electronic (small depletion) charge carriers in the vicinity of the contact. Importantly, this extreme situation resulted in the highest $\beta \approx 23$ factor, which otherwise has been found in the range 5–10. The β factor seems to depend on the electric field even though no simple analytical expression has been obtained so far.

The occurrence of significant field screening in order for the mobile ions to affect the overall current requires a minimum value of mobile ion concentration. This can be estimated from the fact that the depletion zone, proportional to the L_D in Equation (2), cannot be thicker than the distance between electrodes ($w < L$); then

**ADVANCED
SCIENCE NEWS**

www.advancedsciencenews.com

pssrrl

physica status solidi

www.pss-rapid.com

$$N_{ion} > \beta^2 \frac{\varepsilon_0 \varepsilon_r k_B T}{q^2 L^2} \tag{3}$$

Equation (3) shows that this minimum ion concentration depends on the dielectric and geometrical properties of the perovskite, although some voltage dependency may be intrinsically connected to the β factor. Purposely, the values for the minimum N_{ion} are illustrated in Figure S7a, Supporting Information.

The externally imposed drift force for mobile ions can be estimated as $F_d = QV/L$, where Q is the ion charge. However, the effective screening force due to mobile ions can be approximated as $F_s \approx QV/w$, which can be rewritten using Equation (1) as

$$F_s \approx \frac{QL}{\mu_{ion}\tau} \tag{4}$$

Notably, the fact that $F_s > F_d$ suggests that the dynamics of the ionic charge carriers is dominated by the screening mechanism, which motivates us to introduce the effective mobile ion screening acceleration

$$g = \frac{L^2 \varepsilon_0 \varepsilon_r k_B T}{q^2 \tau^2} \tag{5}$$

as a figure of merit for characterizing the slow ionic-mediated current saturation. The definition of Equation (5) can be easily accessed by means of the τ parameterization and **Figure 4** illustrates typical values as a function of the distance between electrodes.

The acceleration of Equation (5) can be deduced from Equation (4) by taking the effective mobile ion mass as

$$m_{eff, ion} = \frac{Qq^2\tau}{\mu_{ion}\varepsilon_0\varepsilon_r k_B T L} \tag{6}$$

Note that this effective mass (see Figure S7b, Supporting Information) is significantly larger than the corresponding absolute values expected from typical single ions composing metal halide perovskites (see Table S3, Supporting Information).
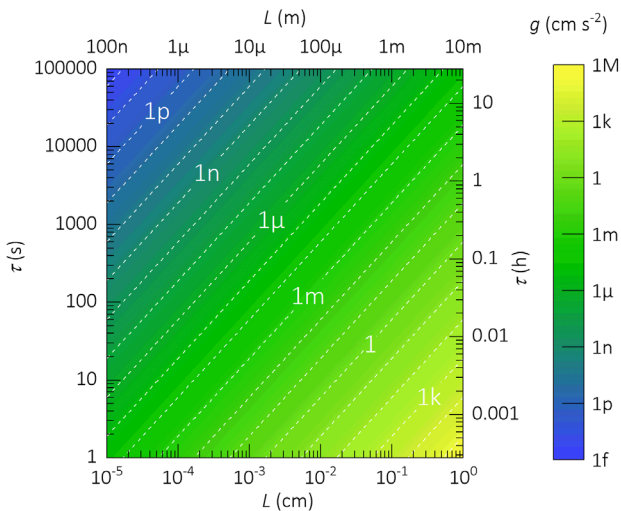
In other words, the dynamics of the mobile ions is defined by the lattice and binding energies rather than their nominal mass. Moreover, provided a value for g and the ion mobility, the mobile ion concentration can be estimated with the accuracy of the β parameter as

$$N_{ion} = \frac{g\beta^2}{\mu_{ion}^2 V^2} \tag{7}$$

Figure S7c, Supporting Information, illustrates characteristic values of the effective mobile ion concentration as a function of the mobility and acceleration. The direct proportionality between g and N_{ion} can be used as a characterization tool for both the saturation and the ion-activation currents. In other words, even though an accurate estimation of the value of N_{ion} may be challenging, samples with reasonably similar ion mobility can be identified to have higher or lower ion concentration throughout the examination of g.

Overall, we stress the importance of preventing the so-called dark current drift[37] by characterizing the perovskite ionic properties of XRDs, and particularly in X-ray imaging. The faster the current response, the better is the image quality and the lower is the required radiation dose, which is of most importance in medical imaging.[33] More importantly, high sensitivity requires low dark saturation current[38] which is hindered by the ionic reordering of the charge density profile. The higher the ionic-related field screening, the higher and slower are the dark saturation current, the higher is the dark shot noise,[39] and the lower is the performance of the PXDs.

4. Conclusions

The time-dependent solutions of the transport equation of a model perovskite-based X-ray detector has been obtained with the aid of the driftfusion[34] open source code. Our simulations of the long-term reverse bias current response to bias voltage polarization can reproduce the main experimental trends,[10,12] including the herein defined regimes of ionic activation and electronic current final saturation. The ionic activation regime is an intermediate process that typically occurs in the time window between milliseconds and tens of seconds where the current can be fully ionic in the presence of sufficient concentration of mobile ions. The transit to the saturation current is the slowest process whose time is directly related with the mobile ion mobility and the screening of the electric field. The final steady-state current under polarization is totally electronic current with a major bulk field-free diffusion component, even though the final distribution of mobile ions and its concentration are determining factors. The reduction of the final current saturation time is shown to appear either by decreasing the perovskite thickness or by increasing the field, the ion concentration, or the mobile ion mobility. More importantly, our simulations suggest that material engineering could be used to prevent the abrupt depletion of mobile ions toward the electrode for smaller and faster reverse bias saturation current. For instance, the screening reduction could be either achieved by modification of the perovskite composition for tuning the mobility and/or concentration of the migrating ions, and/or by including sequences of perovskite/ion-blocking interlayers toward the interfaces hindering the

Figure 4. Simulated effective mobile ion acceleration due to screening, as in Equation (5) with $T = 330$ K and $\varepsilon_r = 28$.[40]

formation of large depletion/accumulation zones. Moreover, the field screening process can be parameterized by means of the ion acceleration as a figure of merit for evaluating ion dynamics. Notably, even though our focus is set on X-ray detectors, our results can also be extended to the study of ion kinetics in similar metal halide perovskite-based semiconductor devices, such as photovoltaic solar cells, light-emitting diodes, and light detectors.

Supporting Information

Supporting Information is available from the Wiley Online Library or from the author.

Conflict of Interest

The authors declare no conflict of interest.

Data Availability Statement

The data that support the findings of this study are available from the corresponding author upon reasonable request.

[1] L. Basiricò, A. Ciavatti, B. Fraboni, *Adv. Mater. Technol.* **2021**, *6*, 2000475.

[2] F. Zhou, Z. Li, W. Lan, Q. Wang, L. Ding, Z. Jin, *Small Methods* **2020**, *4*, 2000506.

[3] O. Almora, D. Baran, G. C. Bazan, C. Berger, C. I. Cabrera, K. R. Catchpole, S. Erten-Ela, F. Guo, J. Hauch, A. W. Y. Ho-Baillie, T. J. Jacobsson, R. A. J. Janssen, T. Kirchartz, N. Kopidakis, Y. Li, M. A. Loi, R. R. Lunt, X. Mathew, M. D. McGehee, J. Min, D. B. Mitzi, M. K. Nazeeruddin, J. Nelson, A. F. Nogueira, U. W. Paetzold, N.-G. Park, B. P. Rand, U. Rau, H. J. Snaith, E. Unger, et al., *Adv. Energy Mater.* **2021**, *11*, 2102526.

[4] C. Eames, J. M. Frost, P. R. F. Barnes, B. C. O'Regan, A. Walsh, M. S. Islam, *Nat. Commun.* **2015**, *6*, 7497.

[5] W. Tress, J. Phys, *Chem. Lett.* **2017**, *8*, 3106.

[6] H.-S. Kim, N.-G. Park, J. Phys, *Chem. Lett.* **2014**, *5*, 2927.

[7] E. L. Unger, E. T. Hoke, C. D. Bailie, W. H. Nguyen, A. R. Bowring, T. Heumuller, M. G. Christoforo, M. D. McGehee, *Energy Environ. Sci.* **2014**, *7*, 3690.

[8] H. J. Snaith, A. Abate, J. M. Ball, G. E. Eperon, T. Leijtens, N. K. Noel, S. D. Stranks, J. T.-W. Wang, K. Wojciechowski, W. Zhang, *J. Phys. Chem. Lett.* **2014**, *5*, 1511.

[9] M. García-Batlle, O. Baussens, S. Amari, J. Zaccaro, E. Gros-Daillon, J.-M. Verilhac, A. Guerrero, G. Garcia-Belmonte, *Adv. Electron. Mater.* **2020**, *6*, 2000485.

[10] M. García-Batlle, S. Deumel, J. E. Huerdler, S. F. Tedde, A. Guerrero, O. Almora, G. Garcia-Belmonte, *ACS Appl. Mater. Interfaces* **2021**, *13*, 35617.

[11] M. García-Batlle, J. Mayen-Guillen, M. Chapran, O. Baussens, J. Zaccaro, J.-M. Verilhac, E. GrosDaillon, A. Guerrero, O. Almora, G. Garcia-Belmonte, *ACS Energy Lett.* **2022**, *7*, 946.

[12] M. García-Batlle, S. Deumel, J. E. Huerdler, S. F. Tedde, O. Almora, G. Garcia-Belmonte, *Adv. Photonics Res.* **2022**, 2200136, https://doi.org/10.1002/adpr.202200136.

[13] D. Moia, I. Gelmetti, P. Calado, W. Fisher, M. Stringer, O. Game, Y. Hu, P. Docampo, D. Lidzey, E. Palomares, J. Nelson, P. R. F. Barnes, *Energy Environ. Sci.* **2019**, *12*, 1296.

[14] O. Almora, G. J. Matt, A. These, A. Kanak, I. Levchuk, S. Shrestha, A. Osvet, C. J. Brabec, G. Garcia-Belmonte, *J. Phys. Chem. Lett.* **2022**, *13*, 3824.

[15] M. Burgelman, P. Nollet, S. Degrave, *Thin Solid Films* **2000**, *361–362*, 527.

[16] M. Zeman, J. van den Heuvel, M. Kroom, J. Willemen, B. Pieters, J. Krc, S. Solntsev, Advanced Semiconductor Analysis (ASA), https://www.tudelft.nl/en/ewi/over-de-faculteit/afdelingen/electrical-sustainable-energy/photovoltaic-materials-and-devices/software-platform/asa-software (accessed: July 2022).

[17] M. A. D. Maur, G. Penazzi, G. Romano, F. Sacconi, A. Pecchia, A. D. Carlo, *IEEE Trans. Electron Devices* **2011**, *58*, 1425.

[18] S. Michael, P. Michalopoulos, presented at *The 2002 45th Midwest Symp. on Circuits and Systems, 2002. MWSCAS-2002*, Yulsa, OK, August 2002.

[19] B. Ruhstaller, T. Beierlein, H. Riel, S. Karg, J. C. Scott, W. Riess, *IEEE J. Sel. Top. Quantum Electron* **2003**, *9*, 723.

[20] O. Almora, J. Wiegand, P. López-Varo, G. J. Matt, C. J. Brabec, *Solar RRL* **2021**, *5*, 2100024.

[21] S. van Reenen, M. Kemerink, H. J. Snaith, *J. Phys. Chem. Lett.* **2015**, *6*, 3808.

[22] G. Richardson, S. E. J. O'Kane, R. G. Niemann, T. A. Peltola, J. M. Foster, P. J. Cameron, A. B. Walker, *Energy Environ. Sci.* **2016**, *9*, 1476.

[23] D. A. Jacobs, Y. Wu, H. Shen, C. Barugkin, F. J. Beck, T. P. White, K. Weber, K. R. Catchpole, *Phys. Chem. Chem. Phys.* **2017**, *19*, 3094.

[24] N. E. Courtier, G. Richardson, J. M. Foster, *Appl. Math. Model.* **2018**, *63*, 329.

[25] S. Almosni, L. Cojocaru, D. Li, S. Uchida, T. Kubo, H. Segawa, *Energy Technol.* **2017**, *5*, 1767.

[26] N. E. Courtier, J. M. Cave, J. M. Foster, A. B. Walker, G. Richardson, *Energy Environ. Sci.* **2019**, *12*, 396.

[27] N. E. Courtier, J. M. Cave, A. B. Walker, G. Richardson, J. M. Foster, *J. Comput. Electron.* **2019**, *18*, 1435.

[28] D. Walter, A. Fell, Y. Wu, T. Duong, C. Barugkin, N. Wu, T. White, K. Weber, *J. Phys. Chem. C* **2018**, *122*, 11270.

[29] M. T. Neukom, A. Schiller, S. Züfle, E. Knapp, J. Ávila, D. Pérez-del-Rey, C. Dreessen, K. P. S. Zanoni, M. Sessolo, H. J. Bolink, B. Ruhstaller, *ACS Appl. Mater. Interfaces* **2019**, *11*, 23320.

2200336 (7 of 8)

[30] S. E. J. O'Kane, G. Richardson, A. Pockett, R. G. Niemann, J. M. Cave, N. Sakai, G. E. Eperon, H. J. Snaith, J. M. Foster, P. J. Cameron, A. B. Walker, *J. Mater. Chem. C* **2017**, *5*, 452.

[31] D. Moia, I. Gelmetti, P. Calado, Y. Hu, X. Li, P. Docampo, J. de Mello, J. Maier, J. Nelson, P. R. F. Barnes, *Phys. Rev. Appl.* **2022**, https://journals.aps.org/prapplied/accepted/ef077K71E9c 1540b35709f4355d4866e9a0eeb38b.

[32] D. A. Jacobs, H. Shen, F. Pfeffer, J. Peng, T. P. White, F. J. Beck, K. R. Catchpole, *J. Appl. Phys.* **2018**, *124*, 225702.

[33] S. Deumel, A. van Breemen, G. Gelinck, B. Peeters, J. Maas, R. Verbeek, S. Shanmugam, H. Akkerman, E. Meulenkamp, J. E. Huerdler, M. Acharya, M. García-Batlle, O. Almora, A. Guerrero, G. Garcia-Belmonte, W. Heiss, O. Schmidt, S. F. Tedde, *Nat. Electron.* **2021**, *4*, 681.

[34] P. Calado, I. Gelmetti, B. Hilton, M. Azzouzi, J. Nelson, P. R. F. Barnes, *J. Comput. Electron.* **2022**, *21*, 960.

[35] R. van Heerden, P. Procel, L. Mazzarella, R. Santbergen, O. Isabella, *Front. Photon.* **2022**, *3*, 889837.

[36] T. Zhang, C. Hu, S. Yang, *Small Methods* **2020**, *4*, 1900552.

[37] J. Peng, Y. Xu, F. Yao, Q. Lin, *Nanoscale* **2022**, *14*, 9636.

[38] X. Xu, W. Qian, S. Xiao, J. Wang, S. Zheng, S. Yang, *EcoMat* **2020**, *2*, 12064.

[39] Y. Xu, Q. Lina, *Appl. Phys. Rev.* **2020**, *7*, 011315.

[40] O. Almora, P. Lopez-Varo, K. T. Cho, S. Aghazada, W. Meng, Y. Hou, C. Echeverría-Arrondo, I. Zimmermann, G. J. Matt, J. A. Jiménez-Tejada, C. J. Brabec, M. K. Nazeeruddin, G. Garcia-Belmonte, *Sol. Energy Mater. Sol. Cells* **2019**, *195*, 291.